




Cite this: *EES Catal.*, 2024,  
2, 675

# Novel double-layer core–shell photocatalyst CdS–TiO<sub>2</sub>@NH<sub>2</sub>-MIL-101: enhanced conversion of CO<sub>2</sub> and CH<sub>4</sub> at ambient temperature†

Yufei Huang,<sup>a</sup> Ling Tan,<sup>a</sup> Hanyu Ma,<sup>b</sup> Xuan Wang,<sup>c</sup> Yangqiang Huang,<sup>\*a</sup>  
Jinping Yin,<sup>c</sup> Zhiwu Liang <sup>\*a</sup> and Xiao Luo <sup>\*a</sup>

The conversion of CO<sub>2</sub> and CH<sub>4</sub> into high value-added chemical products by chemical means is regarded as an emerging industrial technology to solve the increasingly serious climate and energy crises. The solar-powered conversion of CO<sub>2</sub> and CH<sub>4</sub> to syngas is one such technology that holds promise for the production of renewable fuels. Here, ternary core–shell CdS–TiO<sub>2</sub>@NH<sub>2</sub>-MIL-101 composites were prepared using mild experimental methods and their physical and chemical properties were studied using a series of characterization methods. In addition, the interaction between the coupling of different mass fractions of MOF, TiO<sub>2</sub>, and CdS and the performance of photocatalytic, photothermal, and thermocatalytic CH<sub>4</sub> reforming were investigated. The results show that the yields of CO and H<sub>2</sub> of the CdS–TiO<sub>2</sub>@NH<sub>2</sub>-MIL-101 catalyst at room temperature are 364.46 μmol g<sup>−1</sup> and 100.43 μmol g<sup>−1</sup>, respectively, which are 1200–1500% of the catalytic performance of TiO<sub>2</sub>. Moreover, the yields of CO and H<sub>2</sub> of the CdS–TiO<sub>2</sub>@NH<sub>2</sub>-MIL-101 material at 150 °C are 2831.55 μmol g<sup>−1</sup> and 1448.20 μmol g<sup>−1</sup>, respectively. Based on isotope tracer experiments and CO<sub>2</sub> adsorption experiments, a possible comprehensive mechanism for CdS–TiO<sub>2</sub>@NH<sub>2</sub>-MIL-101 photocatalytic CH<sub>4</sub> reforming is proposed. In addition to presenting a fresh research concept for achieving carbon neutrality, this work offers a new technical pathway for the quick conversion of CO<sub>2</sub> and CH<sub>4</sub> at room temperature.

Received 8th November 2023,  
Accepted 3rd January 2024

DOI: 10.1039/d3ey00264k

[rsc.li/eescatalysis](https://rsc.li/eescatalysis)

## Broader context

The traditional thermal catalytic CH<sub>4</sub> reforming process, as we know, has some drawbacks, such as high energy consumption and harsh reaction conditions. It is urgent to develop green and energy-saving CO<sub>2</sub> and CH<sub>4</sub> conversion technologies in light of the world's worsening energy crisis and environmental issues. In this study, the use solar energy to rapidly transform CO<sub>2</sub> and CH<sub>4</sub> at room temperature is proposed in order to reduce the energy consumption cost and break through the thermodynamic limitations of the CH<sub>4</sub> reforming reaction. Here, we designed a novel two-core–shell structure catalyst CdS–TiO<sub>2</sub>@NH<sub>2</sub>-MIL-101, which could achieve rapid conversion of CO<sub>2</sub> and CH<sub>4</sub>. The experimental method of this study provides a new idea for the realization of carbon neutrality and the development of binuclear shell catalysts.

## 1. Introduction

Significantly, the atmospheric concentration of CO<sub>2</sub>, which accounts for more than 50% of the greenhouse effect, has

increased from 280 parts per million (ppm) before the advent of the industrial revolution to approximately 415 ppm now, with an average yearly increase of 2.1 ppm over the previous ten years.<sup>1</sup> As is common knowledge, the effects of global warming include frequent extreme weather events, land desertification, rising sea levels, extinction of wildlife, significant increases in population health and health system risks, and destruction of biodiversity.<sup>2–4</sup> These effects seriously endanger human well-being and the ability to sustainably develop economies. Thus, it is crucial to implement energy conservation and emission reduction in traditional fossil fuel-based industries in order to lower atmospheric CO<sub>2</sub> concentrations and halt the trend of global warming.<sup>5–7</sup>

<sup>a</sup> Joint International Center for CO<sub>2</sub> Capture and Storage (iCCS), The Engineering Research Center of Advanced Catalysis, Ministry of Education Provincial, College of Chemistry and Chemical Engineering, Hunan University, Changsha 410082, P. R. China. E-mail: x\_luo@hnu.edu.cn, yqhuang@hnu.edu.cn, zwliang@hnu.edu.cn

<sup>b</sup> The College of Chinese Language and Literature, Hunan University, Changsha 410082, P. R. China

<sup>c</sup> Shanghai Yanlu Manman Technology Co., Ltd, Shanghai, China

† Electronic supplementary information (ESI) available. See DOI: <https://doi.org/10.1039/d3ey00264k>



Nowadays, CO<sub>2</sub> capture, utilization, and storage technology (CCUS) is one of the essential technologies for greenhouse gas emission reduction and global low-carbon development.<sup>8–10</sup> It has the potential to achieve the efficient exploitation of fossil energy. As one of the active components of greenhouse gases, CH<sub>4</sub> is second only to CO<sub>2</sub> in the damage it causes to the global climate. The conversion of CO<sub>2</sub> and CH<sub>4</sub> into high value-added chemical raw materials could thus simultaneously solve the problems caused by the energy crisis and by the greenhouse effect,<sup>11,12</sup> presenting a feasible solution and the best of both worlds. However, the traditional thermal catalytic conversion of CO<sub>2</sub> and CH<sub>4</sub> has shortcomings, such as a tendency for coking and deactivation of the catalyst, as well as requiring extremely high reaction temperatures, which severely limit its industrial applicability on a broad scale.<sup>13,14</sup> The technology of photocatalytic methane reforming using solar energy had the advantages of a lower reaction temperature, energy saving, and environmental protection, and is regarded as a sustainable emerging method.<sup>15,16</sup> In recent years, numerous researchers have made extremely satisfying scientific progress in the dry reforming of CO<sub>2</sub> and CH<sub>4</sub> with solar energy.

Recently, Laszlo *et al.*<sup>17</sup> investigated the catalytic performance of titanate nanotube (TNT) catalysts loaded with Au and Rh for the photocatalytic conversion of CO<sub>2</sub>–CH<sub>4</sub> at 403 K. It was reported that the yields of H<sub>2</sub> and CO for Au/TNT were increased to 107.25 and 11.9 μmol h<sup>−1</sup> g<sup>−1</sup>, respectively, compared with the blank catalyst TNT. In addition, Tahir *et al.*<sup>18</sup> pointed out that 3% Ag–5% La/PCNNT could convert CH<sub>4</sub> and CO<sub>2</sub> into CO and H<sub>2</sub> at 373 K, with formation rates of CO and H<sub>2</sub> at 312.5 and 62.5 μmol h<sup>−1</sup> g<sup>−1</sup>, respectively. Similarly, Li *et al.*<sup>19</sup> successfully realized the catalytic oxidative coupling reaction of CO<sub>2</sub> and CH<sub>4</sub> under relatively mild experimental conditions using a Ag-supported TiO<sub>2</sub> catalyst, and the yields of CO and C<sub>2</sub>H<sub>4</sub> were 1149 and 686 μmol h<sup>−1</sup> g<sup>−1</sup>, respectively. The number of active sites on catalysts can be significantly increased by grafting precious metals onto semiconductors. However, the use of this technology on a wide scale in industry is severely hampered by the rising cost of raw materials.<sup>20,21</sup> Therefore, some researchers are now focusing on non-precious and metal-free semiconductor materials.

A novel all-solid-state Z-type heterojunction TiO<sub>2</sub>–TiC/g-C<sub>3</sub>N<sub>4</sub> catalyst was investigated by Li *et al.*,<sup>22</sup> and the results revealed that the yields of CO and H<sub>2</sub> under optimal conditions were 11.3 and 2.15 μmol h<sup>−1</sup> g<sup>−1</sup>, respectively. Moreover, Azmat *et al.*<sup>23</sup> investigated the efficiency of the TiO<sub>2</sub>–C<sub>3</sub>N<sub>4</sub>/Ti<sub>3</sub>C<sub>2</sub>TA/R catalyst in the catalytic conversion of CH<sub>4</sub> and CO<sub>2</sub> with the assistance of a concentrator. The results showed that the yields of CO and H<sub>2</sub> reached 87.34 and 51.24 μmol h<sup>−1</sup> g<sup>−1</sup>, respectively. Similarly, Tahir *et al.*<sup>24</sup> reported that the CO and H<sub>2</sub> yields of 2D/2D porous C<sub>3</sub>N<sub>4</sub>–GO composite were 99.75 and 19.52 μmol h<sup>−1</sup> g<sup>−1</sup>, respectively. The C<sub>3</sub>N<sub>4</sub>-modified composite material enhances the transport capacity of photogenerated electrons and hole pairs. Nonetheless, it cannot be denied that this catalyst suffers from issues including low stability and a high recombination rate of photogenerated electrons and hole pairs.<sup>25,26</sup>

NH<sub>2</sub>-MIL-101(Fe), a porous coordination polymer consisting of transition metal ions and organic ligands, has been extensively exploited in the field of photoreduction and CO<sub>2</sub> capture due to its low preparation cost, strong visible light response, porous structure, and other advantages.<sup>27,28</sup> Nevertheless, NH<sub>2</sub>-MIL-101(Fe) still needs to solve the problems of poor stability and the low transport efficiency of photogenerated electron and hole pairs. As an illustration, Dao *et al.*<sup>29</sup> explored the catalytic performance of NH<sub>2</sub>-MIL-101(Fe)/C<sub>3</sub>N<sub>4</sub> composites for CO<sub>2</sub> reduction in solvent-free reactions. Coincidentally, Yuan *et al.*<sup>30</sup> noted that TiO<sub>2</sub>@NH<sub>2</sub>-MIL-88 may effectively convert Cr(VI) in sewage to Cr(III), achieving the purpose of environmental management. Yet, there are very few reports of binary and ternary modified NH<sub>2</sub>-MIL-101 complexes in the field of photocatalytic CH<sub>4</sub> dry reforming.

Herein, different MOF materials were prepared, and the interaction between the coupling of MOFs with different mass fractions of TiO<sub>2</sub> and the photocatalytic CH<sub>4</sub> reforming was explored. Based on this, the photocatalytic performance of the CdS–TiO<sub>2</sub>@MOF ternary hybrid material for the photocatalytic conversion of CO<sub>2</sub> and CH<sub>4</sub> was also investigated. Additionally, the catalytic performance of CdS–TiO<sub>2</sub>@MOF for CH<sub>4</sub> reforming was compared under the experimental conditions of pure light, pure heat, and the photothermal combination. Then, using a variety of characterization techniques, the physicochemical and optoelectronic characteristics of the MOF and its modified composites were investigated. Finally, the possible mechanism of the CdS–TiO<sub>2</sub>@MOF photocatalytic CH<sub>4</sub> reforming reaction is presented in conjunction with the physicochemical characteristics and performance test findings of the catalysts.

## 2. Experimental

### 2.1. Materials and reagents

Detailed information regarding the chemical reagents and related equipment involved in this study is presented in the ESI† S1 Material, and all reagents have not been further purified.

### 2.2. Preparation of the photocatalyst

(1) **Preparation of NH<sub>2</sub>-MIL-101.** The metal–organic framework (MOF) material NH<sub>2</sub>-MIL-101 was prepared by the traditional hydrothermal synthesis reported by Bauer *et al.*<sup>31</sup> Typically, 1.24 mmol of 2-aminoterephthalic acid was placed in beaker A containing 7.5 mL of *N,N* dimethylformamide (DMF) solution, and stirred uniformly for 10 min at room temperature. Similarly, 7.5 mL of DMF solution was added to beaker B, which also contained 2.497 mmol of FeCl<sub>3</sub>·6H<sub>2</sub>O. The mixed solution was stirred at room temperature for 10 min. Then, the liquid in beaker A was added dropwise to beaker B, and the mixture was transferred to a 50 mL hydrothermal reactor. The hydrothermal reactor was then heated for 24 h at 110 °C in the air. The resulting reddish-brown suspension was filtered with a centrifuge and washed three times with DMF solution. Moreover, the washed filter cake was dried in the air at 30 °C and then dried in a vacuum environment at 80 °C for



12 h. Finally, it was sufficiently ground into a powder solid to obtain  $\text{NH}_2\text{-MIL-101}$  (MOF).

(2) **Preparation of  $\text{TiO}_2\text{@NH}_2\text{-MIL-101}$ .**  $\text{TiO}_2$  quantum dots were prepared by a wet chemical method,<sup>32</sup> and the process is shown in S2 Methods (ESI<sup>†</sup>). Here, the preparation process of  $60\text{-TiO}_2\text{@MOF}$  is taken as an example. First, 60 mg of  $\text{TiO}_2$  and 100 mg of MOF were placed in a beaker containing 10 mL of ethanol solution, and sonicated in a water bath for 6–7 h. Next, the mixture was dried under vacuum at 80 °C for 12 h and ground into a solid powder to obtain  $60\text{-TiO}_2\text{@MOF}$  (NFT-60). The preparation processes for the other  $\text{TiO}_2\text{@MOF}$  composites containing different mass fractions of  $\text{TiO}_2$  were similar to that of NFT-60, and the specific steps are shown in S2 Methods (ESI<sup>†</sup>).

(3) **Preparation of  $\text{CdS-TiO}_2\text{@NH}_2\text{-MIL-101}$ .** CdS quantum dots were prepared by a hydrothermal synthesis, according to the literature with slight modifications,<sup>33</sup> and the process can be found in S2 Methods (ESI<sup>†</sup>). Additionally, the  $\text{CdS-TiO}_2\text{@MOF}$  ternary hybrid material was prepared by an ultrasonic drying method (Scheme 1a), and the specific preparation steps are similar to those for NFT-60.

### 2.3. Photocatalytic activity measurements

The photocatalytic performance of the catalyst was evaluated in terms of the  $\text{CO}$  and  $\text{H}_2$  yields at room temperature, and a schematic diagram of the experimental device is shown in Scheme 1b. Typically,  $\text{CO}_2$  and  $\text{CH}_4$  feed gases were passed through a gas mixer unit. The ultrafine glass fiber membrane,

which served as the interface between the photocatalyst and the gas, was then covered with 50 mg of solid catalyst. After that, the photocatalytic performance measurements were carried out for 4 h under exposure to a high-pressure xenon lamp (300 W) to simulate sunlight. Notably, there was no external heat source used in any of the tests, and the feed pressure in the reactor was 40 kPa, controlled by the vacuum pump and the intake valve. Finally, in order to assess the experimental data more precisely and minimize errors, the reaction products were transported online to a gas chromatograph every 0.5 h, which was equipped with FID and TCD detection systems.

### 2.4. Characterization

The structure, morphology, physicochemical properties, and optoelectronic properties of the catalysts were studied by a series of characterization means. Relevant experimental methods and equipment information are presented in S3 Characterization of Catalysts (ESI<sup>†</sup>).

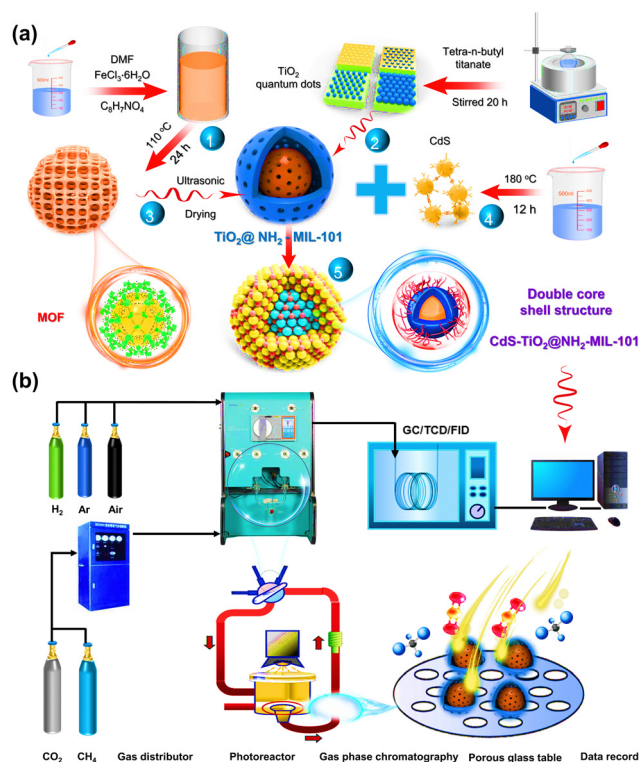
### 2.5. Computational details

In this work, all the theoretical computational models were based on density functional theory and were carried out on the Vienna Ab initio Software Package (VASP). The detailed calculation details can be found in S5 and Fig. S7–S13 (ESI<sup>†</sup>).

## 3. Results and discussion

### 3.1. Structure and morphology analysis

Powder X-ray diffraction (XRD) patterns of  $\text{TiO}_2$ ,  $\text{NH}_2\text{-MIL-101}$ , and  $\text{CdS-TiO}_2\text{@NH}_2\text{-MIL-101}$  are displayed in Fig. 1a. It could be found that  $\text{NH}_2\text{-MIL-101}$  exhibited characteristic peaks at  $8.9^\circ$ ,  $10.3^\circ$ ,  $16.4^\circ$ ,  $20.2^\circ$ , and  $24.5^\circ$ , which were consistent with the data reported in the literature,<sup>29,34,35</sup> indicating that the pure phase  $\text{NH}_2\text{-MIL-101}$  material was successfully prepared. Furthermore, the characteristic peaks



**Scheme 1** (a) Schematic diagram of the process for preparing the ternary composites; (b) process flow equipment diagram for photocatalytic  $\text{CH}_4$  dry reforming.

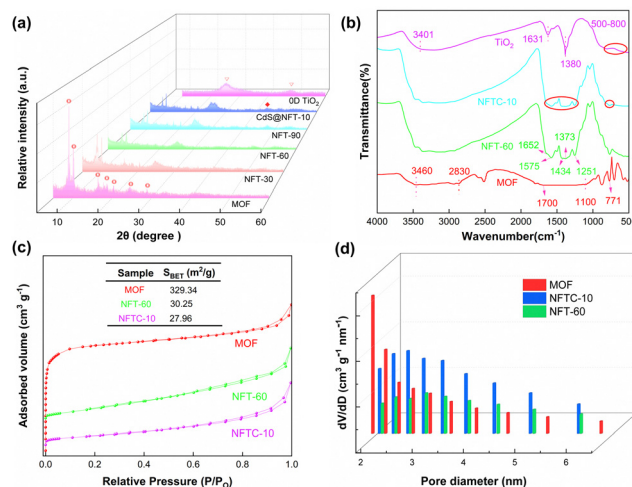


**Fig. 1** (a) XRD patterns of the samples, (b) FT-IR spectra of the catalysts, (c)  $\text{N}_2$  adsorption-desorption isotherms of the MOF and hybrid materials; (d) particle-size distributions of the catalysts.





of  $\text{TiO}_2$  at  $25.34^\circ$  and  $48.04^\circ$  could also be observed.<sup>36–38</sup> It is worth noting that the  $\text{TiO}_2@\text{NH}_2\text{-MIL-101}$  catalyst displayed the characteristic peaks of both  $\text{NH}_2\text{-mil-101}$  and  $\text{TiO}_2$ . The intensity of the MOF-specific characteristic peaks in the NFT material diminished as the mass fraction of  $\text{TiO}_2$  increased, which was the opposite of what happened with  $\text{TiO}_2$ . This indicated the successful introduction of  $\text{TiO}_2$  into the skeleton architecture of MOF. Moreover,  $\text{CdS-TiO}_2@\text{NH}_2\text{-MIL-101}$  showed new characteristic peaks at  $26.2^\circ$  and  $43.9^\circ$ ,<sup>39,40</sup> compared with NFT-60. These resulted from the interaction of CdS with  $\text{TiO}_2@\text{NH}_2\text{-MIL-101}$ , indicating that CdS was uniformly dispersed on the surface of  $\text{TiO}_2@\text{NH}_2\text{-MIL-101}$ .

The functional group structure on the photocatalyst's surface was investigated by Fourier-transform infrared (FT-IR) spectroscopy experiments, and the outcomes are depicted in Fig. 1b and Fig. S1 (ESI<sup>†</sup>). For the MOF, it could be observed that absorption bands appeared at  $771$  and  $1700\text{ cm}^{-1}$ , which were attributed to the vibration of the carboxylic acid group.<sup>41</sup> The peaks at  $1100$  and  $2830\text{ cm}^{-1}$  might be related to the stretching vibrations of C–O and C–H.<sup>31</sup> In addition, the absorption peak at  $3460\text{ cm}^{-1}$  corresponded to the asymmetric stretching vibration of C–N in the amino group. The absorption band of pure  $\text{TiO}_2$  between  $500\text{--}800\text{ cm}^{-1}$  was caused by the stretching vibrations of Ti–O and Ti–O–Ti.<sup>42</sup> The symmetric stretching vibration mode of the carboxyl group was thought to be responsible for the peak at  $1380\text{ cm}^{-1}$ . The characteristic peaks of  $\text{TiO}_2$  at  $1631$  and  $3401\text{ cm}^{-1}$  were related to the stretching vibration of O–H in lattice water. It is worth noting that the absorption peaks of NFT-60 at  $1251$  and  $1575\text{ cm}^{-1}$  were ascribed to the stretching vibration of C–N and the asymmetric stretching vibration of O–C=O, respectively.<sup>43</sup> Additionally, the characteristic peaks located at  $771$ ,  $1373$ , and  $1652\text{ cm}^{-1}$  were assigned to the vibration of the carboxylic acid group. However, the characteristic peak intensity of NFT between  $1200$  and  $1700\text{ cm}^{-1}$  decreased as the mass fraction of  $\text{TiO}_2$  in the hybrid material increased (Fig. S1, ESI<sup>†</sup>). A similar situation emerged with the introduction of CdS into the backbone structure of NFT-60. Here, it may be that a new chemical bond was formed between the metal oxide and the MOF, breaking the original structure of MOF.

The microstructural properties of the catalysts, such as the specific surface area, particle size, and micro-mesoporous volume, were investigated by carrying out  $\text{N}_2$  adsorption and desorption experiments, and the results are presented in Fig. 1c. All of the adsorption isotherms of the prepared materials were found to contain hysteresis loop structures,<sup>44,45</sup> which were typical IV isotherms, indicating that the materials had mesoporous and microporous structures. Here, the specific surface areas of the MOF, NFT-60, and NFTC-10 were  $329.34$ ,  $30.25$ , and  $27.96\text{ m}^2\text{ g}^{-1}$ , respectively. The sharp reduction of the specific surface area of the binary or ternary hybrid materials may be related to the dispersion of  $\text{TiO}_2$  and CdS onto the surface or into the pores of the MOF.

This speculation was further supported by the catalyst's pore volume and particle size. Fig. 1d and Fig. S2 (ESI<sup>†</sup>) show that the pure MOF had an average particle size and pore capacity of

$2.11\text{ nm}$  and  $0.23\text{ cm}^3\text{ g}^{-1}$ , respectively. Nevertheless, the average particle sizes and pore volumes of NFT-60 and NFTC-10 were  $0.10$  and  $0.09\text{ cm}^3\text{ g}^{-1}$  and  $3.15$  and  $4.17\text{ nm}$ , respectively. Moreover, the MOF itself contained microporous particle sizes, while NFT-60 and NFTC-10 catalysts had virtually no microporous particle sizes. The above data indicate that  $\text{TiO}_2$  and CdS had been uniformly dispersed on the surface or in the pores of MOF.

Scanning electron microscopy (SEM) experiments were carried out to investigate the morphologies of  $\text{NH}_2\text{-mil-101}$ ,  $\text{TiO}_2@\text{NH}_2\text{-MIL-101}$ , and  $\text{CdS-TiO}_2@\text{NH}_2\text{-MIL-101}$ , and the corresponding results are presented in Fig. 2 and Fig. S3 (ESI<sup>†</sup>). It could be distinctly observed that a single MOF had a regular octahedral structure,<sup>46,47</sup> as displayed in Fig. 2a, b and Fig. S3a (ESI<sup>†</sup>). The morphology of the MOF was greatly changed after the introduction of  $\text{TiO}_2$  into the framework of the MOF. Additionally, NFT-60 had a morphology similar to that of an asymmetric ellipse or sphere with a layer of tiny solid particles on top. The consistent  $\text{TiO}_2$  coating on the surface of the MOF was to blame for this. Yet, the irregularity of the morphology of NFT increased with the mass fraction of  $\text{TiO}_2$  in NFT, which was related to the complete wrapping of  $\text{TiO}_2$  on the surface of the MOF (Fig. S3, ESI<sup>†</sup>). After the further grafting of CdS on to NFT-60, it was found that the morphology of  $\text{CdS-TiO}_2@\text{NH}_2\text{-MIL-101}$  resembled a solid doughnut structure, filled with different solid small particles on the outermost and in the middle. In addition, the elemental distribution on the surface of the NFTC-10 catalyst was assessed by EXD mapping (Fig. S4, ESI<sup>†</sup>). The results show that three metal elements, namely Cd, Ti, and Fe, could be detected on the surface of the NFTC-10 material, demonstrating the successful introduction of  $\text{TiO}_2$  and CdS into the framework structure of the MOF.

The transmission electron microscopy (TEM) images of the MOF and the composite materials are displayed in Fig. 3 and Fig. S5 (ESI<sup>†</sup>). The MOF was found to possess an octahedral structure, which was confirmed by SEM. Fig. 3b and c show that

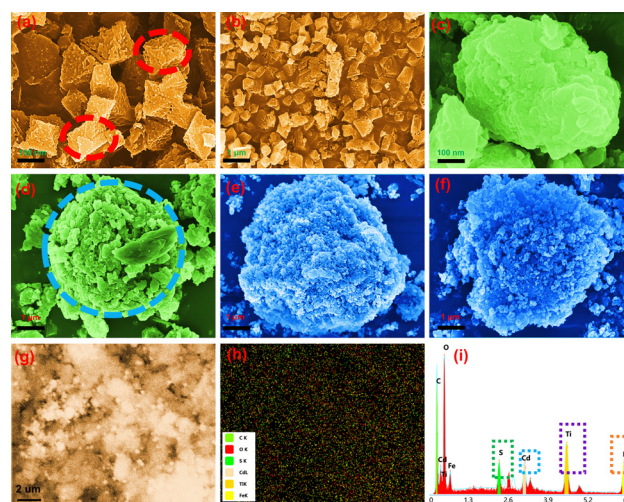


Fig. 2 (a)–(f) SEM images of catalysts; (g)–(i) EDX mapping images of NFTC-10.



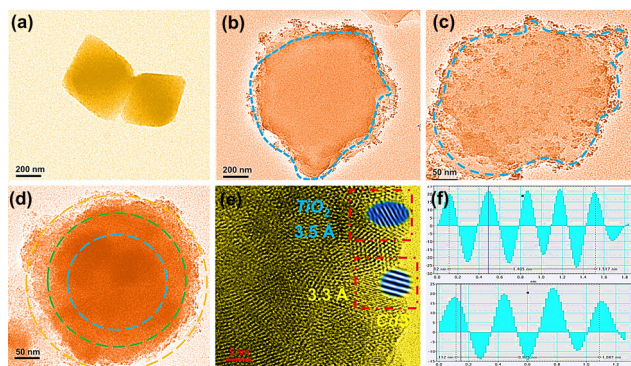


Fig. 3 TEM images of core-shell-structured catalysts: ((a) MOF; (b) NFT-30; (c) NFT-60; (d) NFTC-10; (e) HR-TEM image of NFTC-10; (f) crystal plane spacing diagram of NFTC-10).

TiO<sub>2</sub> was uniformly wrapped around the surface of the MOF, forming irregular ellipsoidal spheres. The CdS was further loaded on the composite NFT-60, and it was observed that NFTC-10 formed concentric circular patterns with three layers of different shades of color. The SEM characterization results were identical to this, demonstrating that CdS was effectively grafted onto the composite. The boundary interfaces of MOF with TiO<sub>2</sub> and CdS could be seen in the HR-TEM micrographs of NFTC-10, and the crystal plane spacings of TiO<sub>2</sub> and CdS were calculated, as shown in Fig. 3e, f, and Fig. S5d (ESI<sup>†</sup>). The spacing of the lattice stripes of CdS and TiO<sub>2</sub> were 0.32 and 0.35 nm, which fitted well with the (002) crystal plane of CdS and the (101) crystal plane of TiO<sub>2</sub>,<sup>48,49</sup> respectively.

The elemental composition and valence of the surface of the photocatalyst were studied by X-ray photoelectron spectroscopy (XPS), and the results are presented in Fig. 4. As shown in Fig. 4a, the elements C, N, O, and Fe were found in the full spectra of MOF, NFT-60, and NFTC-10. Apart from these, the Ti element was detected in the NFT-60 sample, and Ti, Cd, and S elements were detected in NFTC-10, indicating that the metal semiconductor was successfully grafted on the surface or in the pores of the MOF. In the high-resolution Fe 2p spectrum (Fig. 4b), the characteristic peaks of the MOF observed at 711.6 and 726.4 eV corresponded to Fe 2p<sub>3/2</sub> and Fe 2p<sub>1/2</sub>,<sup>50,51</sup>

respectively. The characteristic peaks at 714.0, 718.5, 723.5, and 730.1 eV were the satellite peaks of Fe 2p<sub>3/2</sub> and Fe 2p<sub>1/2</sub>, attributed to the high spin of the Fe (Fe<sup>3+</sup>) compound.<sup>52</sup> The introduction of TiO<sub>2</sub> and CdS into the structure of the MOF revealed a slight negative shift in the high-resolution spectral peaks of NFT-60 and NFTC-10 compared with that in the Fe 2p spectrum of MOF. This shift was related to the increase in electron cloud density of Fe<sup>3+</sup> ions, whereupon the semiconductor forms a chemical bond with the NH<sub>2</sub> group, causing the lone electron pair on the N atom to shift toward the Fe<sup>3+</sup> ions.<sup>53</sup> The Ti 2p map of TiO<sub>2</sub>@NH<sub>2</sub>-MIL-101 showed characteristic peaks at 458.9 and 464.7 eV (Fig. 4c), which were related to the spin-orbit splitting photoelectronic activity of the Ti 2p<sub>1/2</sub> and Ti 2p<sub>3/2</sub> chemical states of Ti<sup>4+</sup>.<sup>54–56</sup> However, the peak of the characteristic energy spectrum of CdS-TiO<sub>2</sub>@NH<sub>2</sub>-MIL-101 showed a slight shift to the right, which may be related to the interaction of Cd with the NH<sub>2</sub> group.

Additionally, the Cd 3d spectrum displayed two different spectral peaks located at 405.7 and 412.6 eV (Fig. 4d), which were assigned to the Cd 3d<sub>5/2</sub> and Cd 3d<sub>3/2</sub> orbitals of Cd,<sup>57,58</sup> respectively. Four peaks at 248.8, 286.3, 288.9, and 291.0 eV were visible in the MOF C1 XPS patterns, indicating the existence of C–C, C–N, and C=O bonds in the MOF.<sup>51,59</sup> (Fig. 4e). Yet, the characteristic peak energy band values of the composite were slightly shifted to the right. As shown in Fig. 4f, the N1s XPS spectrum indicated the presence of –NH<sub>2</sub> (399.7 eV), N–C=O (401.1 eV), and –N–H<sup>+</sup> (426.6 eV) chemical bonds in the MOF.<sup>60,61</sup> However, the N1s characteristic peaks of TiO<sub>2</sub>@MOF and CdS-TiO<sub>2</sub>@MOF exhibited a slight negative shift, and a different satellite peak appeared in the 404–410 eV region. Here, it is possible that the grafted metal formed a chemical bond with N and the interaction between the organic ligands formed a  $\pi$ - $\pi^*$  bond, resulting in a shift of the main nitrogen peak to the left by a few eV.<sup>62</sup>

### 3.2. Photocatalytic activities analysis

Electrochemical studies were used to explore the photoelectric characteristics of the catalysts, including the absorbance and photoresponse of the materials.<sup>63,64</sup> The results are displayed in Fig. 5. Generally, for semiconductor materials, the greater the photocurrent response intensity, the stronger the separation ability of photogenerated electrons. It was noted that here that the MOF material alone had a weaker photocurrent response. Fortunately, grafting TiO<sub>2</sub> on the MOF could significantly improve the photocurrent response intensity of the composites. Among the MOFs, NFT-60 had the highest photocurrent response intensity among all the binary composites. Also, the ternary hybrid material produced from combining CNT-60 and a small amount of CdS exhibited a significant change in the light-response intensity, and it was almost four times that of CNT-60. The above data indicate that the introduction of CdS and TiO<sub>2</sub> could significantly enhance the separation rate of photogenerated electrons and hole pairs in the CdS-TiO<sub>2</sub>@NH<sub>2</sub>-MIL-101 composites.

Moreover, in the impedance pattern, the radius of the arc of the Nyquist curve is related to the resistance of the charge

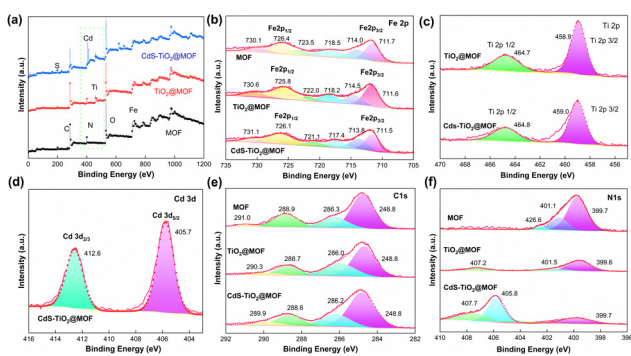


Fig. 4 XPS spectra of the MOF, TiO<sub>2</sub>@NH<sub>2</sub>-MIL-101, and CdS-TiO<sub>2</sub>@NH<sub>2</sub>-MIL-101 materials: (a) survey scan, Fe 2p (b), Ti 2p (c), Cd 3d (d), C 1s (e), and N 1s (f).





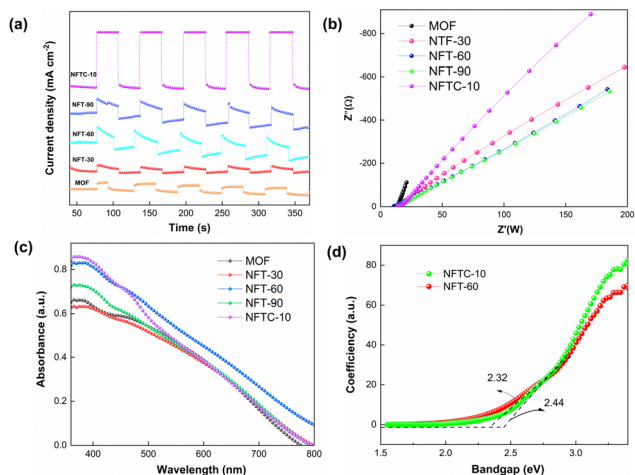


Fig. 5 (a) Transient photocurrent of the catalysts; (b) EIS spectra of the MOF and composite materials; (c) UV-vis diffuse reflection spectra of the samples; (d) band gap energies of the hybrid materials.

transfer, and a smaller radius corresponds to a lower transfer resistance.<sup>65,66</sup> From Fig. 5b, it is evident that the arc radius of the MOF was the largest, followed by those of NFTC-10 and NFT-30. It is worth noting that NFT-60 and NFT-90 had the smallest arc radii. This indicates that TiO<sub>2</sub> supported on the MOF materials could improve the transmission rate of TiO<sub>2</sub>@NH<sub>2</sub>-MIL-101 electrons, while CdS grafting had a negative effect.

The UV-vis diffuse-reflectance experiments were conducted to investigate the light-absorption capacity of the catalysts, and the results are presented in Fig. 5(c and d) and Fig. S6 (ESI†). The MOF had a strong absorbance in the wavelength range of 380–500 nm. When a tiny amount of TiO<sub>2</sub> was loaded on the MOF, it was found that the absorbance intensity of NFT-30 in the ultraviolet region decreased, but the absorbance capacity of NFT-30 in the visible region increased. By further increasing the mass fraction of TiO<sub>2</sub> in the MOF, the absorbance of the hybrid material at 380–800 nm was significantly enhanced. Among the binary hybrids, NFT-60 exhibited the best light-absorption ability, followed by that of NFT-90. Interestingly, when introducing a slight amount of CdS into the structure of NFT-60, it was observed that the absorbance of CdS-TiO<sub>2</sub>@NH<sub>2</sub>-MIL-101 was diminished at 380–430 nm, but significantly increased at 430–800 nm. It could be observed from Fig. 5d and Fig. S6 (ESI†) that the band gaps of MOF, NFT-60, and NFTC-10 were 2.52, 2.32, and 2.44 eV, respectively, suggesting the interaction between TiO<sub>2</sub>, CdS, and MOF may change the band gap width of the composite. Also, the reason is that the light-absorption ability of the different hybrid materials was different.

### 3.3. Catalytic performances of the catalysts

**3.3.1. Photocatalytic performance.** The photocatalytic CH<sub>4</sub> reforming performance of the MOF, TiO<sub>2</sub>, and TiO<sub>2</sub>@MOF catalysts was evaluated by the yields of CO and H<sub>2</sub>, and the results are shown in Fig. 6. From Fig. 6a, it could be seen that the CO yield of TiO<sub>2</sub> within 4 h was 31.16 μmol g<sup>-1</sup>. The CO

yields of NH<sub>2</sub>-MIL-Al and NH<sub>2</sub>-MIL-101(Fe) were 54.60 and 126.72 μmol g<sup>-1</sup>, respectively, which were 175% and 407% higher than the catalytic performance of TiO<sub>2</sub>. On this basis, the photocatalytic performance of the composite of TiO<sub>2</sub> and NH<sub>2</sub>-MIL-101 with different masses of TiO<sub>2</sub> was studied, as shown in Fig. 6b. Here, the CO yield of NFT-30 was 291.76 μmol g<sup>-1</sup>. Importantly, the catalytic performance of the MOF could be greatly enhanced by the addition of TiO<sub>2</sub>. The photocatalytic performance of the TiO<sub>2</sub>@NH<sub>2</sub>-MIL-101 hybrid material was greatly enhanced as the mass fraction of TiO<sub>2</sub> increased. When the mass of TiO<sub>2</sub> was 60%, NFT-60 achieved the optimal catalytic performance, and the yield of CO was 468.24 μmol g<sup>-1</sup>. Then, the catalytic performance of NFT-90 followed closely, and the CO yield was 376.45 μmol g<sup>-1</sup>.

Impressively, the H<sub>2</sub> yields of NFT-30, NFT-60, and NFT-90 were 3.88, 8.77, and 6.82 μmol g<sup>-1</sup>, respectively. The H<sub>2</sub> yields of TiO<sub>2</sub>@NH<sub>2</sub>-MIL-101, however, fell short of expectations. This might be associated with the water-gas shift reaction and the kind of active sites that the catalyst's exposure revealed. Nevertheless, it could still be proven that NFT-60 had the best catalytic efficiency among the five catalysts, and it was 1500% and 370% higher than that of TiO<sub>2</sub> and MOF, respectively. A small quantity of CdS was next supported on the surface of the binary hybrid material NFT-60 to address this weakness and boost the effectiveness of the composite catalyst for the catalytic conversion of CH<sub>4</sub>. Fig. 6d demonstrates that a small amount of CdS could considerably boost the H<sub>2</sub> production in the composite catalyst. Here, the H<sub>2</sub> yield of 5%-CdS/TiO<sub>2</sub>@NH<sub>2</sub>-MIL-101 was 84.92 μmol g<sup>-1</sup>. Fortunately, the hydrogen yield of 10%-CdS/TiO<sub>2</sub>@NH<sub>2</sub>-MIL-101 was as high as 100.43 μmol g<sup>-1</sup>, which was almost 1200% more than that of TiO<sub>2</sub>@NH<sub>2</sub>-MIL-101. However, as the mass of the CdS increased, the catalytic efficacy of the CdS/TiO<sub>2</sub>@NH<sub>2</sub>-MIL-101 catalyst declined. The most obvious sign of this was that the hydrogen yield of 15%-CdS/TiO<sub>2</sub>@NH<sub>2</sub>-MIL-101 was 64.78 μmol g<sup>-1</sup>.

Additionally, it could be seen that the CO yields of NFTC-5, NFTC-10, and NFTC-15 were 312.88, 364.46, and 218.98 μmol g<sup>-1</sup>, respectively (Fig. 6c). Nevertheless, the CO yield of the ternary hybrid material was slightly decreased compared with the

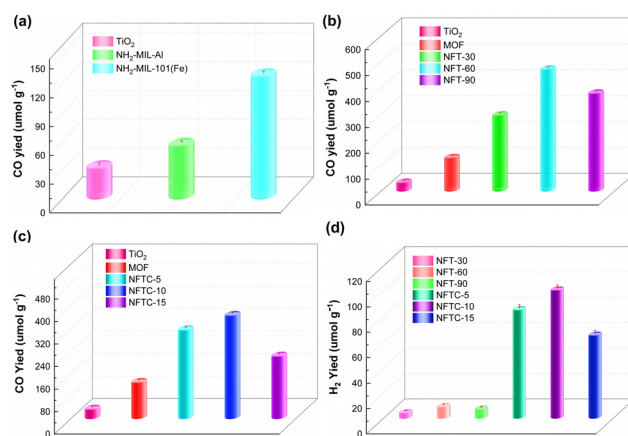


Fig. 6 CO and H<sub>2</sub> yield rates of various samples (4 h).



catalytic performance of  $\text{TiO}_2\text{@NH}_2\text{-MIL-101}$ . Based on the above data, it is clear that the introduction of CdS could enhance the activation of the C–H bond in  $\text{CH}_4$  and increase the production of  $\text{H}_2$ . Meanwhile, the process of CdS and  $\text{TiO}_2$  compounding with the MOF enhanced the light-response intensity of the semiconductor. The recombination rate of electrons and holes in the composite material was also improved, which was not conducive to the reduction of  $\text{CO}_2$ , resulting in a decrease in the yield of CO.

**3.3.2. Photothermal catalysis.** The effect of temperature on the performance of NFTC-10 in photocatalytic  $\text{CH}_4$  reforming was investigated using a fixed-bed reactor under continuous feed conditions, and the results are shown in Fig. 7. From Fig. 7(a and b), it could be observed that the yields of  $\text{H}_2$  were 55.71 and 57.15  $\mu\text{mol g}^{-1}$  for NFTC-10 under intermittent and continuous feeding conditions, respectively, while the yields of CO were 298.65 and 119.7  $\mu\text{mol g}^{-1}$ , respectively. The difference in catalytic performance may be related to the amounts of reactants adsorbed on the catalyst surface and the concentration of  $\text{CO}_2$  and  $\text{CH}_4$  in the system. Here, the catalytic performance of NFTC-10 was significantly improved when the temperature of the fixed-bed reactor was raised to 150  $^\circ\text{C}$  (Fig. 7(c and d)), and the yields of  $\text{H}_2$  and CO were 1448.20 and 2831.55  $\mu\text{mol g}^{-1}$ , respectively, which were 25.34 and 23.66 times higher than the catalytic performance of NFT-10 at room temperature. Here, the interaction between light and heat reduces the activation energy barrier of the reaction between  $\text{CH}_4$  and  $\text{CO}_2$ , and significantly improves the catalytic efficiency of NFTC-10.

Therefore, the catalytic performance of NFTC-10 for  $\text{CH}_4$  dry reforming at different temperatures was also investigated in this work, as displayed in Fig. 8. The CO yield of NFTC-10 was 28  $\text{mmol g}^{-1}$  at 600  $^\circ\text{C}$ . Its catalytic performance though improved with the increase in temperature. At 750  $^\circ\text{C}$ , the yield of CO of NFTC-10 reached a maximum of 471.62  $\text{mmol g}^{-1}$ . The catalytic performance of NFTC-10 initially increased but subsequently declined with the temperature in terms of the production of  $\text{H}_2$ ;

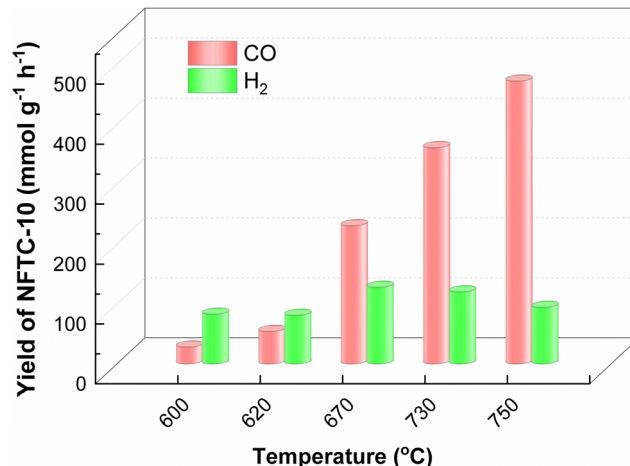


Fig. 8 Effect of temperature on the conversion of  $\text{CO}_2$  and  $\text{CH}_4$  catalyzed by NFTC-10.

whereby the  $\text{H}_2$  yield of NFTC-10 was 82.92  $\text{mmol g}^{-1}$  at 600  $^\circ\text{C}$ , reaching a maximum value of 127.93  $\text{mmol g}^{-1}$  at 670  $^\circ\text{C}$ , but then decreasing to 94.34  $\text{mmol g}^{-1}$  with further increasing the temperature. It may be the case here that the higher temperature increased the rate of the side reaction of water-gas conversion, thus reducing the production of  $\text{H}_2$ . The large energy input facilitated the activation of  $\text{CH}_4$  with  $\text{CO}_2$  and increased the reaction rate for dry reforming of methane. In addition, the ternary hybrid materials designed in this work achieved excellent catalytic performance in photocatalytic methane reforming and thermocatalytic methane reforming.

**3.3.3. Stability analysis.** The NFTC-10 photocatalytic  $\text{CH}_4$  reforming experiment was carried out continuously for 24 h to investigate the stability of the catalyst, and the results are presented in Fig. 9. Remarkably, the catalytic performance of NFTC-10 decreased significantly after three cycles of experiments. Thereafter, the yield of CO increased slowly with the increment in the reaction time. The catalytic activity of NFTC-10 essentially disappeared after the sixth cycle. The yield of  $\text{H}_2$  per unit time declined as the reaction time increased. After 24 h of continuous operation, the CO and  $\text{H}_2$  yields of NFTC-10 were 500 and 139  $\mu\text{mol g}^{-1}$ , respectively. The above data indicate that the catalytic performance of NFTC-10 seriously degraded after six cycles of experiments. Therefore, it was necessary to explore the cause of this deactivation.

The structure and photoelectrochemical properties of the cycled catalysts were investigated with four characterization methods (Fig. 9(c–f)). As can be observed in Fig. 9c, the FT-IR patterns of the fresh and cycled catalysts had slightly different peaks at 1200–1700  $\text{cm}^{-1}$ . The cycled catalyst displayed a new characteristic peak at 1200–1700  $\text{cm}^{-1}$ , which may be the result of the carboxylic acid group and O–C=O vibration. The results show that some intermediates were adsorbed on the active site of the catalyst during the dry reforming of methane, which resulted in the deactivation of the catalyst. In addition, the light-response intensity of both cycled catalysts NFT-60 and NFTC-10 decreased, compared to the fresh catalysts (Fig. 9d).

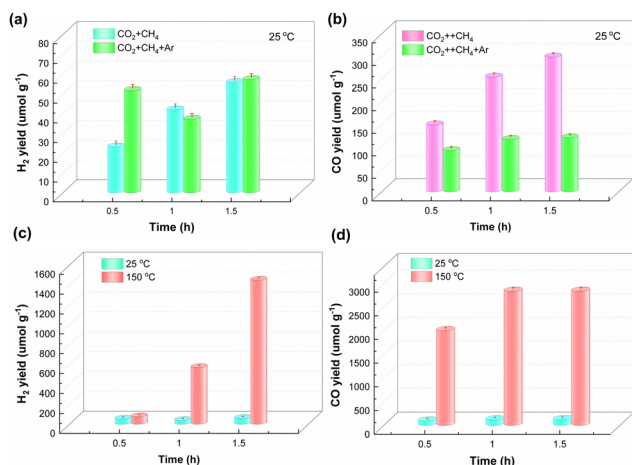


Fig. 7 Performance of NFTC-10 in photothermal catalytic methane reforming.



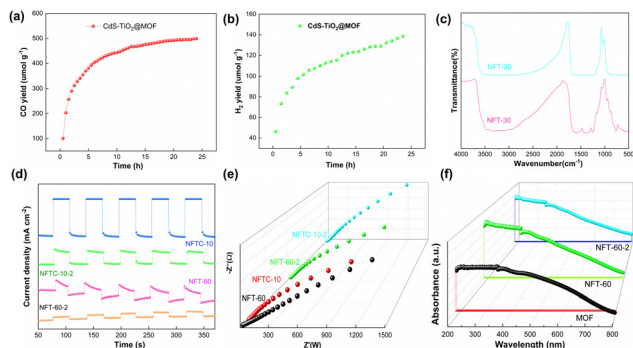


Fig. 9 Cyclic performance test of the NFTC-10 catalyst (a) and (b), yields of CO and H<sub>2</sub>; (c) FT-IR spectra; (d) I-T; (e) and (f), EIS and UV-vis diffuse reflection spectra; respectively).

The EIS experiments demonstrated that the impedance value of the circulating catalyst became smaller, indicating a faster compounding rate of photogenerated electrons and holes (Fig. 9e). It could also be observed from Fig. 9f that the light-absorption capacity of the NFT-60 catalyst also decreased after light exposure. From the above experimental data, it is shown that the carbon accumulation of the catalyst, the decrease in light-absorption capacity, and the acceleration of the photo-generated electron-hole complexation rate are critical causes of photocatalytic deactivation.<sup>67</sup>

### 3.4. Investigating the structure-functional relationships

Here, in order to better explore the interaction between the coupling between TiO<sub>2</sub> and CdS distributed on the surface of the MOF and the renormalization performance of CH<sub>4</sub>, the energy barrier changes of some intermediates during the reaction of CO<sub>2</sub> and CH<sub>4</sub> were calculated by DFT. The CO<sub>2</sub> adsorption and activation models of TiO<sub>2</sub>@NH<sub>2</sub>-MIL-101 and CdS/TiO<sub>2</sub>@NH<sub>2</sub>-MIL-101 are shown in Fig. 10a. It can be observed from Fig. 10b that the TiO<sub>2</sub>@NH<sub>2</sub>-MIL-101 catalyst could significantly reduce the activation energy of CO<sub>2</sub> to the intermediates HOCO\* and \*CO (\*CO<sub>2</sub>\* → \*HOCO\*, −0.28 eV; \*HOCO\* → \*CO; −0.27 eV). When CdS was introduced to the surface of TiO<sub>2</sub>@NH<sub>2</sub>-MIL-101, it was found that the activation energy of CO<sub>2</sub> to the intermediates \*HOCO\* and CO\* increased significantly (\*CO<sub>2</sub>\* → \*HOCO\*, 0.29 eV; \*HOCO\* → \*CO; 0.23 eV). This indicated that the synergistic effect of TiO<sub>2</sub> and NH<sub>2</sub>-MIL-101 can actively promote the activation of the C=O double bond in CO<sub>2</sub>. However, CdS will weaken the activation of TiO<sub>2</sub> and NH<sub>2</sub>-MIL-101 on CO<sub>2</sub> to a certain extent. The results show that the active site exposed by TiO<sub>2</sub> is conducive to the conversion of CO<sub>2</sub>. The introduction of CdS covered part of the TiO<sub>2</sub> active sites, resulting in a decrease in CO production.

Additionally, the influence of different catalysts on the reaction energy barrier of the C-H bonds in the CH<sub>4</sub> dehydrogenation process was investigated (Fig. 11). It can be observed from Fig. 11b that as the deep dehydrogenation of CH<sub>4</sub> increased, more energy was required during the reaction. The reaction energy barrier for the complete dehydrogenation of CH<sub>4</sub> on the MOF was 19.40 eV (CH<sub>4</sub>  $\xrightarrow{x(h^+)}$  C deposit + xH<sup>+</sup>).

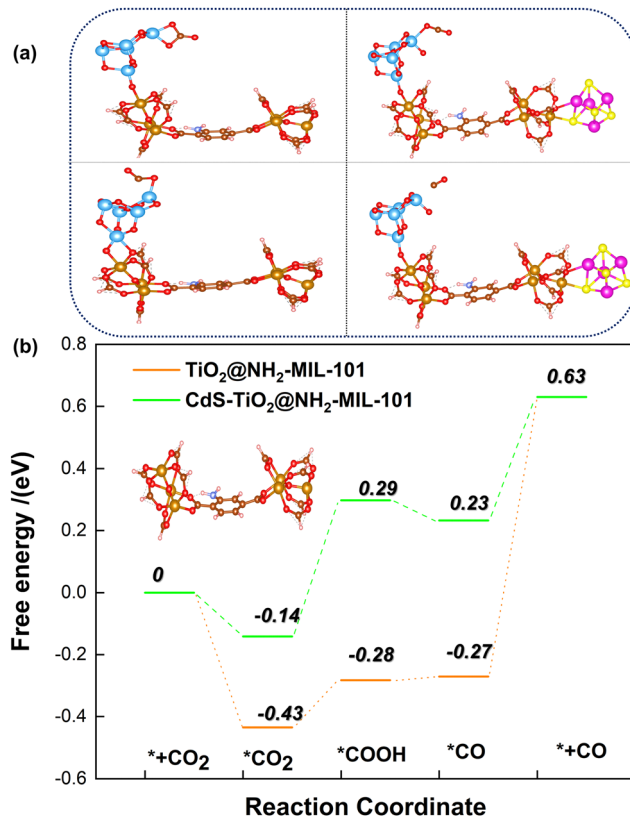


Fig. 10 Energy barrier change diagram of CO<sub>2</sub> to CO photocatalyzed by the MOF-based composite catalysts.

Introducing TiO<sub>2</sub> into the MOF could reduce the reaction energy barrier of CH<sub>4</sub> to \*C (CH<sub>4</sub>  $\xrightarrow{x(h^+)}$  C deposit + xH<sup>+</sup>; 16.67 eV). The synergistic catalysis of CdS with TiO<sub>2</sub> and the MOF could significantly reduce the total reaction energy barrier of CH<sub>4</sub> to \*C (CH<sub>4</sub>  $\xrightarrow{x(h^+)}$  C deposit + xH<sup>+</sup>; 16.00 eV). The above calculations show that CdS plays a crucial role in C-H activation during CH<sub>4</sub> dehydrogenation. The theoretical calculations were in high agreement with the experimental results.

The changes of the functional groups on the surface of the NFTC-10 catalyst during the photocatalytic CH<sub>4</sub> reforming process were studied by *in situ* DRIFTS characterization experiments (Fig. 12), which provided a theoretical basis for the possible catalytic mechanism. It can be observed from Fig. 12 that the absorption peaks of CO<sub>2</sub> (2340 and 2360 cm<sup>−1</sup>) and CH<sub>4</sub> (1302 and 3013 cm<sup>−1</sup>) on the catalyst surface gradually decreased with the increment in the reaction time. The absorption peak at 1330 cm<sup>−1</sup> was attributed to the asymmetric stretching vibration of \*CH<sub>3</sub>. The absorption peaks at 1653 and 1740 cm<sup>−1</sup> were related to the asymmetric tensile vibrations of \*COOH and \*CHO, respectively. The weaker absorption peaks at 1925 and 2155 cm<sup>−1</sup> were attributed to the asymmetric stretching vibrations of \*CO and C=O in CO. It is worth noting that the peaks intensity of \*CO and CO were relatively low, which may be related to the reaction time. Moreover, the strength of the absorption peaks at 3505 and 3667 cm<sup>−1</sup>





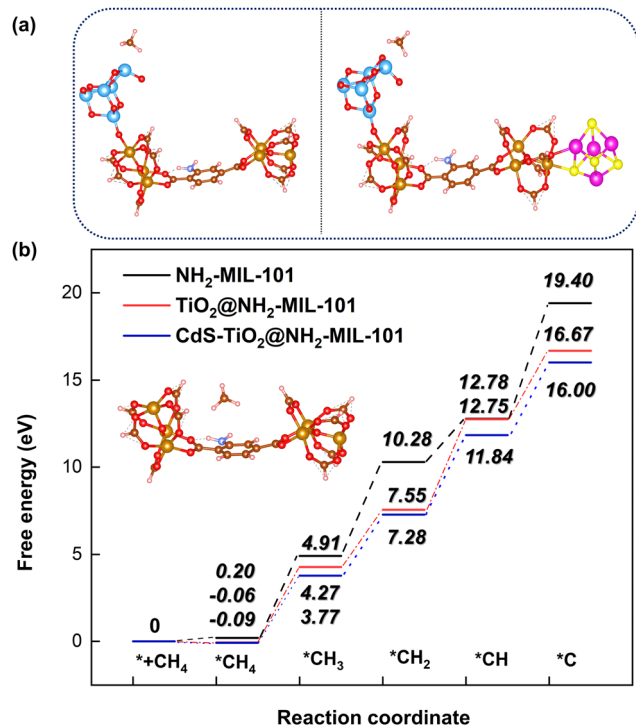


Fig. 11 Energy barrier change diagram for the photocatalytic dehydrogenation of  $\text{CH}_4$  reforming with the MOF-based composite catalysts.

increased with time, which was caused by the stretching vibration of  $-\text{OH}$ .

### 3.5. Possible catalytic mechanism

Fig. 13 illustrates the results of isotopic tracer studies using  $^{13}\text{C}$ -labeled  $\text{CO}_2$  to investigate the origin of C in the product  $\text{CO}$  and to provide evidence for the investigation of a potential catalytic  $\text{CH}_4$  dry reforming mechanism. As observed in the mass spectra of Fig. 13a, the product  $\text{CO}$  showed only one peak at the mass-to-charge ratio  $m/z = 28$  with  $^{12}\text{CO}_2$  as the reactant. The  $\text{CO}_2$  reduction studies used  $^{13}\text{CO}_2$  that had been  $^{13}\text{C}$ -labeled, and  $\text{CO}$  showed separate characteristic peaks at  $m/z = 28$  and  $m/z = 29$ , which were attributed to  $^{12}\text{CO}$  and  $^{13}\text{CO}$ , respectively. The isotope tracing experiments demonstrated that C in the reaction product  $\text{CO}$  was derived from  $\text{CO}_2$  and  $\text{CH}_4$ , respectively.

The  $\text{CO}_2$  adsorption of the composite catalyst was investigated by thermogravimetry, and the results are shown in Fig. 14. The  $\text{CO}_2$  adsorption amount of MOF after 40 min was  $0.43 \text{ mmol g}^{-1}$ . However, the  $\text{CO}_2$  adsorption amount of NFT-30 was  $0.33 \text{ mmol g}^{-1}$ . The  $\text{CO}_2$  adsorption amount of the NFT composites decreased with the increase in  $\text{TiO}_2$  loading. It could also be found that the adsorption amounts of NFT-60 and NFT-90 were  $0.28$  and  $0.24 \text{ mmol g}^{-1}$ , respectively. It is known that the amino group and porous physical structure of the MOF was conducive to the adsorption of  $\text{CO}_2$  and  $\text{CH}_4$  small molecule gases. The introduction of  $\text{TiO}_2$  into the skeleton structure of the MOF may destroy the porous structure of the MOF, which is not conducive to the adsorption of  $\text{CO}_2$ .

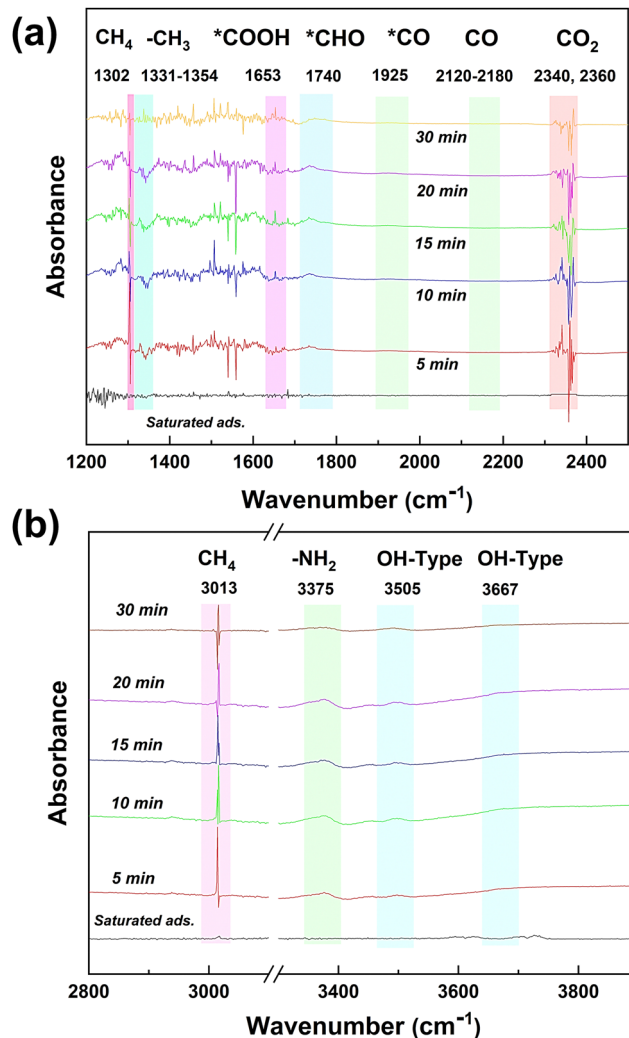


Fig. 12 *In situ* DRIFTS spectra of chemical substances and intermediates in the photocatalytic  $\text{CH}_4$  reforming process by  $\text{CdS}/\text{TiO}_2@ \text{NH}_2\text{-MIL-101}$  catalysts.

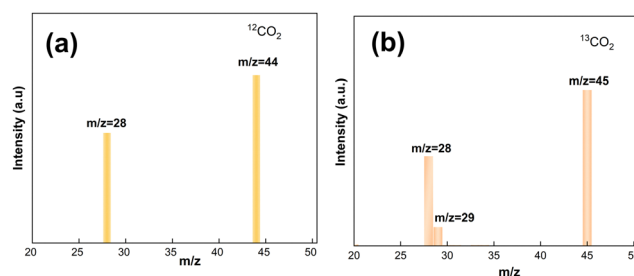


Fig. 13 Isotopic mass spectrometry analysis of the carbon products.

A possible catalytic mechanism for the dry reforming of  $\text{CH}_4$  by NFTC is postulated, as illustrated in Fig. 15, by combining the characterization, performance test studies, and isotope tracing investigations results. First, the reactants are fixed in the pore or on the surface of the catalyst under the action of van der Waals force and physical adsorption.



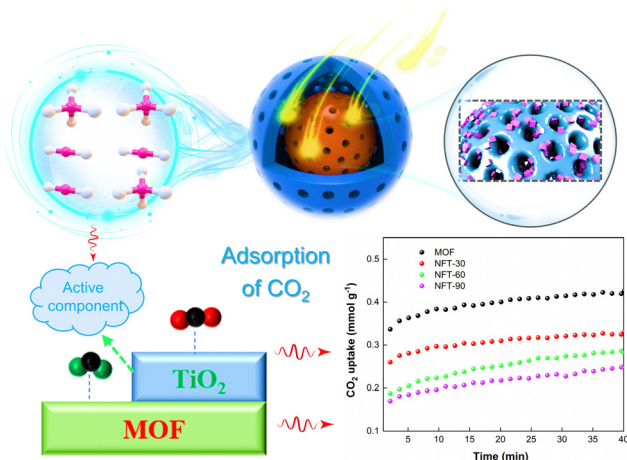
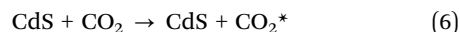
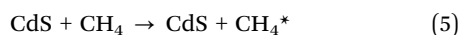
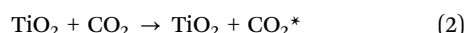
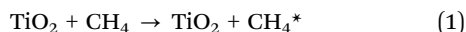


Fig. 14 CO<sub>2</sub> adsorption schematic and performance curves for TiO<sub>2</sub>@NH<sub>2</sub>-MIL-101.

The specific adsorption process is shown in eqn (1)–(6) and Fig. 14.

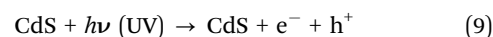
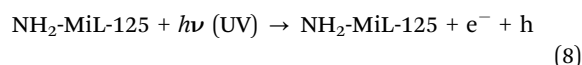
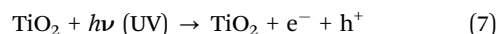
**a. Adsorption on the catalysts:**



When the energy of the incident light is greater than the band gap ( $E_g$ ) of the semiconductor, the electrons located in the valence band of the semiconductor can transition to the conduction band of the semiconductor after absorbing the energy of the photon (steps 7–9). Here, electrons are excited and transferred from the organic ligand of the MOF to the Fe–O cluster, leaving behind holes. Some of the photogenerated electrons on the MOF surface are compounded with holes on

the TiO<sub>2</sub> conduction band by the built-in electric field and diffusion, forming a specific heterojunction structure, which in turn accelerates the directional electron motion (Fig. 15a). Since the energy bands of CdS match each other with the energy bands of NH<sub>2</sub>-MIL-101, a modest amount of CdS quantum dots dispersed on the surface of TiO<sub>2</sub>@NH<sub>2</sub>-MIL-101 with a core-shell structure can further enhance the photoresponse intensity of the composite and accelerate the transport rate of photogenerated electrons and holes.

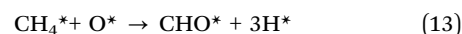
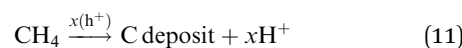
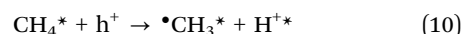
**b. Photoexcitation:**



The electrons and holes on the surface of the composite can undergo redox reactions with CO<sub>2</sub> and CH<sub>4</sub> (Fig. 15b). The deep oxidation of CH<sub>4</sub> can produce the intermediate products C\* and H<sup>+</sup>, and C\* combines with O\* from the reduction of CO<sub>2</sub> to form CO\* (steps 10–12). Moreover, CH<sub>4</sub>\* can also be combined with O\* to generate CHO\* and H\* (step 13). Then, CHO\* can further generate CO\* and H\* (step 14). Two H<sup>+</sup> can produce hydrogen with the help of electrons. CO can be directly generated by CO<sub>2</sub> interacting with the photogenerated electrons. In addition, CO<sub>2</sub> can produce intermediate products, such as •CO<sub>2</sub>\*<sup>−</sup>, O\*, •HOCO\*<sup>−</sup>, after several reductions (steps 17–19). The structure of •HOCO\*<sup>−</sup> is unstable and easily decomposes into CO\* and OH<sup>−</sup> (step 20). OH<sup>−</sup> can bind to H<sup>+</sup> on the surface of the catalyst to form H<sub>2</sub>O (step 21). Finally, the generated products are desorbed from the surface of the material or from the pores (steps 22–24).

**c. Reaction and desorption:**

(1) Oxidation of CH<sub>4</sub>:



(2) Reduction of CO<sub>2</sub>:

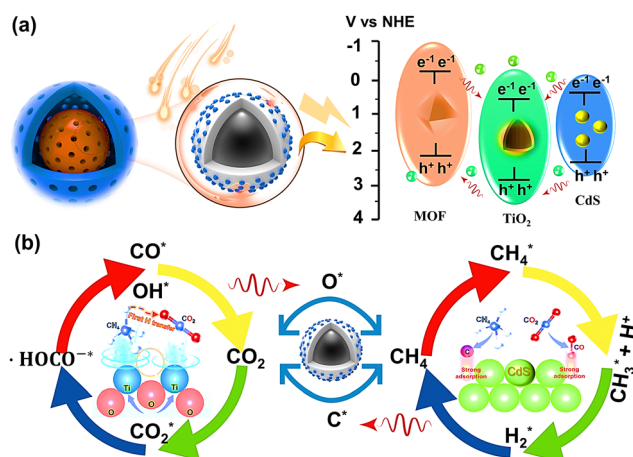
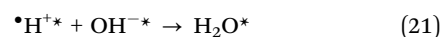
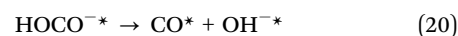
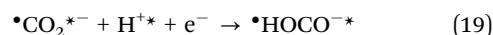
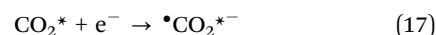


Fig. 15 Schematic diagram of possible catalytic mechanisms.



## (3) Desorption:



## 4. Conclusion

The binary and ternary composites  $\text{TiO}_2@\text{NH}_2\text{-MIL-101}$  and  $\text{CdS-TiO}_2@\text{NH}_2\text{-MIL-101}$  were prepared by an ultrasonic drying method, and their physical and chemical properties were investigated by characterization with XRD, FT-IR, SEM, TEM, I-T, and UV/vis techniques. Then, the performances of 10 different catalysts in the dry reforming of  $\text{CH}_4$  ( $\text{TiO}_2$ ,  $\text{NH}_2\text{-MIL-101}$ ,  $\text{TiO}_2@\text{NH}_2\text{-MIL-101}$ , and  $\text{CdS-TiO}_2@\text{NH}_2\text{-MIL-101}$ ) were investigated. It is worth noting that the CO and  $\text{H}_2$  yields of  $60\text{-TiO}_2@\text{NH}_2\text{-MIL-101}$  were 468.24 and  $8.77 \mu\text{mol g}^{-1}$ , respectively. Impressively, the yields of CO and  $\text{H}_2$  of  $10\text{-CdS-TiO}_2@\text{NH}_2\text{-MIL-101}$  at  $25^\circ\text{C}$  and  $150^\circ\text{C}$  were 364.46, 100.43, 2831.55, and 1448.20  $\mu\text{mol g}^{-1}$ , respectively. The cyclic stability of the  $10\text{-CdS-TiO}_2@\text{NH}_2\text{-MIL-101}$  catalyst was investigated and the causes of its photocatalyst deactivation were explored. Finally, based on the material characterization, performance testing experiments,  $\text{CO}_2$  adsorption experiments, and isotope tracer experiments, a possible mechanism of photocatalytic  $\text{CH}_4$  reforming of ternary heterojunction composites was proposed.

## Author contributions

Z. Liang and Y.-Q. Hung directed and supervised the study. X. Luo proposed innovative research methods, guided the specific implementation plan of this research, and modified the overall writing of the paper. Y. Huang carried out experiments, analyzing experimental data, and completed the writing of the paper. X. Wang and J.-P. Yin established the calculation model, completed all the theoretical calculation simulation experiments. H.-Y. Ma and L. Tan revised and polished the language of the paper.

## Conflicts of interest

The authors declare that they have no known competing financial interests or personal relationships that could have appeared to influence the work reported in this paper.

## Acknowledgements

The financial support from the National Natural Science Foundation of China (No. 22178089).

## Notes and references

- 1 J. Ren, A. Yu, P. Peng, M. Lefler, F.-F. Li and S. J. Licht, *Acc. Chem. Res.*, 2019, **52**, 3177–3187.

- 2 R. Rickaby, *Nature*, 2010, **465**, 849.
- 3 S. J. Davis, K. Caldeira and H. D. Matthews, *Science*, 2010, **329**, 1330–1333.
- 4 W. Wang, K. Zhang, T. Xu and Y. Yao, *Energy Environ. Sci.*, 2022, **51**, 17081–17088.
- 5 A. M. Appel, J. E. Bercaw, A. B. Bocarsly, H. Dobbek, D. L. DuBois, M. Dupuis, J. G. Ferry, E. Fujita, R. Hille and P. J. Kenis, *Chem. Rev.*, 2013, **113**, 6621–6658.
- 6 S. I. Seneviratne, M. G. Donat, A. J. Pitman, R. Knutti and R. L. Wilby, *Nature*, 2016, **529**, 477–483.
- 7 T. Zurrer, E. Lovell, Z. Han, K. Liang, J. Scott and R. Amal, *Energy Environ. Sci.*, 2022, **14**, 15669–15678.
- 8 M. Aresta, A. Dibenedetto and A. Angelini, *Chem. Soc. Rev.*, 2014, **114**, 1709–1742.
- 9 W. Gao, S. Liang, R. Wang, Q. Jiang, Y. Zhang, Q. Zheng, B. Xie, C. Y. Toe, X. Zhu, J. Wang, L. Huang, Y. Gao, Z. Wang, C. Jo, Q. Wang, L. Wang, Y. Liu, B. Louis, J. Scott, A. C. Roger, R. Amal, H. He and S. E. Park, *Chem. Soc. Rev.*, 2020, **49**, 8584–8686.
- 10 Y. Yan, T. N. Borhani, S. G. Subraveti, K. N. Pai, V. Prasad, A. Rajendran, P. Nkulikiyinka, J. O. Asibor, Z. Zhang, D. Shao and E. Science, *Energy Environ. Sci.*, 2021, **14**, 6122–6157.
- 11 L. C. Buelens, V. V. Galvita, H. Poelman, C. Detavernier and G. B. Marin, *Science*, 2016, **354**, 449–452.
- 12 Control methane to slow global warming — fast, *Nature*, 2021, **596**, 461, DOI: [10.1038/d41586-021-02287-y](https://doi.org/10.1038/d41586-021-02287-y).
- 13 S. M. Kim, P. M. Abdala, T. Margossian, D. Hosseini, L. Foppa, A. Armutlulu, W. van Beek, A. Comas-Vives, C. Copéret and C. Müller, *J. Am. Chem. Soc.*, 2017, **139**, 1937–1949.
- 14 M. Akri, S. Zhao, X. Li, K. Zang, A. F. Lee, M. A. Isaacs, W. Xi, Y. Gangarajula, J. Luo, Y. Ren, Y. T. Cui, L. Li, Y. Su, X. Pan, W. Wen, Y. Pan, K. Wilson, L. Li, B. Qiao, H. Ishii, Y. F. Liao, A. Wang, X. Wang and T. Zhang, *Nat. Commun.*, 2019, **10**, 5181.
- 15 A. A. Khan and M. Tahir, *Appl. Catal., B*, 2021, **285**, 119777.
- 16 A. V. Tavasoli, M. Preston and G. Ozin, *Energy Environ. Sci.*, 2021, **14**, 3098–3109.
- 17 L. Balazs and K. Janos, Photoreactions in  $\text{CO}_2\text{-CH}_4$  system on metal modified titanate nanotubes, *LAP-Lambert Academic Publishing*, 2016.
- 18 B. Tahir, M. Tahir and N. Amin, *Appl. Catal., B*, 2019, **248**, 167–183.
- 19 N. Li, R. Jiang, Y. Li, J. Zhou and M. Liu, *ACS Sustainable Chem. Eng.*, 2019, **7**.
- 20 L. Foppa, T. Margossian, S. M. Kim, C. Müller, C. Coperet, K. Larmier and A. Comas-Vives, *J. Am. Chem. Soc.*, 2017, **139**, 17128–17139.
- 21 D. Li, Y. Nakagawa and K. Tomishige, *Appl. Catal., A*, 2011, **408**, 1–24.
- 22 Z. Li, Y. Mao, Y. Huang, D. Wei, M. Chen, Y. Huang, B. Jin, X. Luo and Z. Liang, *Catal. Sci. Technol.*, 2022, **12**, 2804–2818.
- 23 B. Aaka and A. Mt, *Appl. Catal., B*, 2020, **285**.
- 24 B. Rria and A. Mt, *Fuel*, 2021, **305**, 121558.
- 25 H. Li, S. Gan, H. Wang, D. Han and L. Niu, *Adv. Mater.*, 2015, **27**, 6906–6913.





- 26 W. J. Ong, L. L. Tan, Y. H. Ng, S. T. Yong and S. P. Chai, *Chem. Rev.*, 2016, **116**, 7159–7329.
- 27 Y. Wang, H. Fang, S. Liang, X. Sheng, Y. Huang, Y. Zhang and Y. Zhou, *Appl. Surf. Sci.*, 2022, **606**, 154872.
- 28 Y. Wan, H. Yang, Q. Shang, Q. Cheng, H. Zhou and Z. Pan, *Environ. Sci.: Nano*, 2022, **9**, 3081–3093.
- 29 X. Y. Dao, X. F. Xie, X. Y. Zhang, Y. S. Kang and W. Y. Sun, *ACS Appl. Energy Mater.*, 2020, **3**, 3946–3954.
- 30 R. Yuan, C. Yue, J. Qiu, F. Liu and A. Li, *Appl. Catal., B*, 2019, **251**, 229–239.
- 31 S. Bauer, C. Serre, T. Devic, P. Horcajada, J. Marrot, G. R. Ferey and N. Stock, *Inorg. Chem.*, 2008, **47**, 7568–7576.
- 32 Z. Jiang, X. Xu, Y. Ma, H. S. Cho and H. Deng, *Nature*, 2021, **590**, E16.
- 33 H. Yang, C. Yang, N. Zhang, K. Mo and L. Wen, *Appl. Catal., B*, 2020, **285**, 119801.
- 34 X. Li, W. Guo, Z. Liu, R. Wang and H. Liu, *J. Hazard. Mater.*, 2016, **324**, 665–672.
- 35 J. Liu, W. Cheng, K. Zhang, H. Liu, J. Li, J. Tressel and S. Chen, *ACS Appl. Bio Mater.*, 2022, **5**, 3912–3922.
- 36 J. Wang, Y. Shen, S. Liu and Y. Zhang, *Appl. Catal., B*, 2020, **270**, 118885.
- 37 Y. Yu, X. Dong, P. Chen, Q. Geng, H. Wang, J. Li, Y. Zhou and F. Dong, *ACS Nano*, 2021, **15**, 14453–14464.
- 38 Z. Cui, Q. Zhang, H. Fu, Q. Liu, X. Liu, Y. Wu, P. Gao, Z. Wang, Z. Zheng and H. Cheng, *Appl. Catal., B*, 2023, **333**, 122812.
- 39 X. Zheng, Y. Li, J. Yang and S. Cui, *Chem. Eng. J.*, 2021, **422**, 130105.
- 40 H. Yang, C. Yang, N. Zhang, K. Mo, Q. Li, K. Lv, J. Fan and L. Wen, *Appl. Catal., B*, 2021, **285**, 119801.
- 41 B. Mha, A. Wp, Y. A. Yang, S. A. Lang, A. Jc, C. Ak, A. Zz, A. Qf, D. Yt and L. Wei, *J. Colloid Interf. Sci.*, 2021, **599**, 484–496.
- 42 A. Yz, A. Jx, A. Jm, A. Ss, B. Zwa, B. Tl, Y. B. Cheng and A. Zs, *J. Hazard. Mater.*, 2020, **394**, 122529.
- 43 Y. Ma, D. G. Atinafu, G. Hai, W. Dong and G. Wang, *Sci. Bull.*, 2020, **65**.
- 44 S. Zhao, J. Xu, M. Mao, L. Li and X. Li, *J. Colloid Interface Sci.*, 2021, **583**, 435–447.
- 45 Y. H. Zou, Y. B. Huang, D. H. Si, Q. Yin, Q. J. Wu, Z. Weng and R. Cao, *Angew. Chem., Int. Ed.*, 2021, **133**, 21083–21088.
- 46 S. Su, Z. Xing, S. Zhang, M. Du, Y. Wang, Z. Li, P. Chen, Q. Zhu and W. Zhou, *Appl. Surf. Sci.*, 2021, **537**, 147890.
- 47 K. E. Dekrafft, C. Wang and W. Lin, *Adv. Mater.*, 2012, **24**, 2014–2018.
- 48 D. Jiang, L. Zhu, R. M. Irfan, L. Zhang and P. Du, *Chinese J. Catal.*, 2017, **38**, 2102–2109.
- 49 J. Chen, M. Wang, J. Han and R. Guo, *J. Colloid Interface Sci.*, 2020, **562**, 313–321.
- 50 J. Xu, Y. Qi, C. Wang and L. Wang, *Appl. Catal., B*, 2019, **241**, 178–186.
- 51 J. Fu, X. Wang, T. Wang, J. Zhang, S. Guo, S. Wu and F. Zhu, *ACS Appl. Mater. Interfaces*, 2019, **11**, 33238–33244.
- 52 C. Y. Hu, Z. W. Jiang, C. P. Yang, X. Y. Wang, X. Wang, S. J. Zhen, D. M. Wang, L. Zhan, C. Z. Huang and Y. F. Li, *Chem. Eur. J.*, 2022, e202201437.
- 53 X.-Y. Dao, X.-F. Xie, J.-H. Guo, X.-Y. Zhang, Y.-S. Kang and W.-Y. Sun, *ACS Appl. Energy Mater.*, 2020, **3**, 3946–3954.
- 54 H. Wang, X. Yuan, Y. Wu, G. Zeng, X. Chen, L. Leng and H. Li, *Appl. Catal., B*, 2015, **174**, 445–454.
- 55 K. Lan, Y. Liu, W. Zhang, Y. Liu, A. Elzatahry, R. Wang, Y. Xia, D. Al-Dhayan, N. Zheng and D. Zhao, *J. Am. Chem. Soc.*, 2018, **140**, 4135–4143.
- 56 M. Kim, J. Choi, W. Lee, Y.-Y. Ahn, H. Lee, K. Cho and J. Lee, *Appl. Catal., B*, 2023, 122993.
- 57 P. Wang, Y. Mao, L. Li, Z. Shen, X. Luo, K. Wu, P. An, H. Wang, L. Su and Y. Li, *Angew. Chem. Int. Ed.*, 2019, **58**, 11329–11334.
- 58 J. Li, L. Wang, W. Wang, X. Jia, Y. Zhang, H. Yang, Y. Li and Q. Zhou, *Appl. Catal., B*, 2023, **334**, 122833.
- 59 M. Humayun, W. Pi, Y. Yuan, L. Shu, J. Cao, A. Khan, Z. Zheng, Q. Fu, Y. Tian and W. Luo, *J. Colloid Interface Sci.*, 2021, **599**, 484–496.
- 60 S. Qiu, Y. Zhou, X. Ren, B. Zou, W. Guo, L. Song and Y. Hu, *Chem. Eng. J.*, 2020, **402**, 126212.
- 61 S. Wang, Y. Xia, G. Yan, M. Chen, X. Wang, L. Wu and R. Liang, *Appl. Catal., B*, 2022, **317**, 121798.
- 62 G.-M. Rignanes, A. Pasquarello, J.-C. Charlier, X. Gonze and R. Car, *Phys. Rev. Lett.*, 1997, **79**, 5174.
- 63 G. Tang, X. Zeng, L. Hou, T. Song, S. Yin, B. Long, A. Ali and G.-J. Deng, *Appl. Catal., B*, 2022, **306**, 121090.
- 64 X. Liu, L. Yang, M. Huang, Q. Li, L. Zhao, Y. Sang, X. Zhang, Z. Zhao, H. Liu and W. Zhou, *Appl. Catal., B*, 2022, **319**, 121887.
- 65 D. Long, J. Liu, H. Chen, P. Liu, K. Zheng, Y. Zeng, X. Chen, S. Li and M. Lu, *Appl. Catal., B*, 2023, **330**, 122625.
- 66 H. Zhang, S. Si, G. Zhai, Y. Li, Y. Liu, H. Cheng, Z. Wang, P. Wang, Z. Zheng and Y. Dai, *Appl. Catal., B*, 2023, 122909.
- 67 G. E. Schukraft, B. Moss, A. G. Kafizas and C. Petit, *ACS Appl. Mater. Interfaces*, 2022, **14**, 19342–19352.

